

Investigations of the March 2006 African dust storm using ground-based column-integrated high spectral resolution infrared (8–13 μm) and visible aerosol optical thickness measurements:

1. Measurement procedures and results

M. Thomas,¹ C. Gautier,¹ and P. Ricchiazzi¹

Received 4 August 2008; revised 5 February 2009; accepted 24 February 2009; published 4 June 2009.

[1] The infrared (IR) aerosol optical thickness (AOT) spectra of Saharan dust measured during the Portable Infrared Aerosol Transmission Experiment (PIRATE) are reported. Saharan dust optical thickness (extinction) spectra from 8 to 13 μm were obtained using column-integrated solar transmission measurements in Puerto Rico in July 2005 and Senegal in January and March 2006 (during a dust plume) using a Fourier transform infrared (FTIR) spectrometer. The FTIR measured the solar spectral irradiance in the IR in the presence of Saharan dust, and the AOT was determined by comparing the measured spectra to modeled downwelling spectra without dust for the same atmospheric temperature profile, solar zenith angle, water vapor, and ozone concentrations. The modeled dust-free spectra are generated using the Santa Barbara Disort Atmospheric Radiative Transfer (SBDART) program. The measured dust AOT is compared with modeled AOT spectra obtained using Mie theory with dust indices of refraction from Volz and Fouquart with assumed lognormal size distributions. When the visible AOT values from nearby Aerosol Robotic Network (AERONET) sensors are compared to the IR AOT values, results from various dust loadings show that the IR dust AOT at 9.5 μm is typically only one third that of the visible (670 nm) dust AOT, but there is some evidence that this ratio could increase for larger dust size distributions. The surface IR dust forcing is determined to be about -0.4 W/m^2 by summing the dusty and clear irradiance differences.

Citation: Thomas, M., C. Gautier, and P. Ricchiazzi (2009), Investigations of the March 2006 African dust storm using ground-based column-integrated high spectral resolution infrared (8–13 μm) and visible aerosol optical thickness measurements: 1. Measurement procedures and results, *J. Geophys. Res.*, 114, D11202, doi:10.1029/2008JD010928.

1. Introduction

[2] Mineral dust aerosols have a significant impact on the Earth's radiation budget and climate [Forster *et al.*, 2007]. Dust redistributes radiative heating at the surface and in the atmosphere by scattering and absorbing shortwave radiation and by scattering, absorbing and emitting longwave radiation. To monitor dust distributions and their climatic impact, ground and satellite-based observations have been performed [Fraser, 1976; Glaccum and Prospero, 1980; Fouquart *et al.*, 1987a, 1987b; Legrand *et al.*, 1988; Tanre and Legrand, 1991; Jankowiak and Tanre, 1992; Goloub *et al.*, 1999; Hsu *et al.*, 2000; Kaufman *et al.*, 2000; Schmid *et al.*, 2000; Prospero *et al.*, 2002; Sokolik, 2002; Formenti *et al.*, 2003; Highwood *et al.*, 2003; Petit *et al.*, 2005; Slingo *et al.*, 2006]. To date most of the ground-based dust observations have been in the ultraviolet (UV) [Petit *et al.*, 2005], visible (VIS)

and/or near-infrared (NIR) [Moorthy *et al.*, 2001]; however, Agassi *et al.* [2006] reported on measurements of infrared (IR) dust radiance in Israel to discriminate dust from other aerosols, while a more recent paper by Turner [2008] describes measurements in Naimy, Niger of the IR radiance for the same 2006 Saharan dust storm that is the focus of this paper to determine the radiatively significant mineral aerosol composition and size distribution. Satellite-based dust observations have used wavelengths from the UV to the IR. Many satellite-based dust detection and tracking sensors (TOMS, SeaWifs, MODIS, MISR) use UV-NIR wavelengths and primarily track dust over ocean [Tanre *et al.*, 1988; Li, 1995; Mishchenko and Travis, 1997; Goloub *et al.*, 1999; King *et al.*, 1999; Torricella *et al.*, 1999; Guelle *et al.*, 2000; Kaufman *et al.*, 2000; Balkanski *et al.*, 2006; J. E. Conel *et al.*, Ground-based validation of the EOS Multi-angle Imaging SpectroRadiometer (MISR) aerosol retrieval algorithms and science data products, paper presented at IGARSS'97, Inst. of Electr. and Electron. Eng., New York, 1997]. IR is also used in satellite observations of dust (AVHRR, MODIS and AIRS) because IR offers the potential advantages of day and night detection of dust and detection of dust over desert

¹Institute for Computational Earth System Science, Department of Geography, University of California, Santa Barbara, California, USA.

surfaces due to thermal differences between the dust and surface [Legrand *et al.*, 1988, 1989; Ackerman, 1997; Wald *et al.*, 1998].

[3] Although IR detection of dust from space has its advantages, it also has its challenges. One of the principal challenges is the lack of observational data on either the altitude-dependent or column-integrated infrared optical effects of dust [Liao and Seinfeld, 1998; Gasso *et al.*, 2000; Pierangelo *et al.*, 2004]. IR dust detection algorithms for space-based sensors often rely on calculated IR optical properties (extinction, absorption and scattering efficiencies, and asymmetry parameter) based on index of refraction measurements from individual aerosol samples or minerals at discrete wavelengths and Mie calculations based on assumed size distributions and spherical particles of predefined mineralogy [Ackerman and Chung, 1992; Ackerman, 1997; Kaufman, 1987; Marticorena *et al.*, 1997; Mishchenko *et al.*, 1997; Li, 1998; Guelle *et al.*, 2000; Haywood *et al.*, 2001; Perlwitz *et al.*, 2001]. Although these assumptions have been shown to be reasonable in many cases, detailed data of collected Saharan dust show that aerosols are neither spherical in shape nor composed of a uniform mixture of minerals [Kaufman *et al.*, 1997; West *et al.*, 1997; Gao and Anderson, 2001]. Uncertainties have remained regarding whether assumed optical properties of dust based on spherical and mineralogical assumptions for external mixtures accurately represent the optical properties for an ensemble of particle sizes, shapes, minerals, and mixtures. Further uncertainties exist regarding the accuracy of remote dust property retrievals from space using modeled dust properties [Tegen and Fung, 1994; Claquin *et al.*, 1998]. To help reduce these uncertainties, we conducted experiments to directly measure the AOT of Saharan dust plumes in the IR as a function of wavelength.

[4] The main dust plume we investigated was from an African dust storm that originated on 5 March 2006 when anomalously strong northerly winds produced a wide front of dust in northern Algeria. The front propagated southward across the Sahara over the following days, lifting more dust into the atmosphere. Slingo *et al.* [2006] reported that the southward movement of the dust from Algeria appeared to propagate close to the surface, following the lowest terrain and moving around the highest topography (e.g., the Tibesti) or being channeled through mountain passes (in the Hoggar and Air massifs). The dust reached Niamey, Nigeria on 7 March and Dakar, Senegal on 8 March. For the next 5 days dust poured off West Africa and over the Atlantic. Figure 1 shows pictures taken in M'bour, Senegal on 14 January 2006 under relatively clear skies and 9 March 2006 during the dust storm. In the following sections we report on the experimental methods, spectral irradiance calculations, optical thickness calculations, comparisons with the AERONET data and dust models, and discuss the results from measurements made during this and two smaller dust plume events.

2. Experimental Methods

[5] The Portable Infrared Aerosol Transmission Experiment (PIRATE) was a ground-based experiment designed to measure the infrared AOT of mineral aerosols (dust). A Fourier Transform Infrared (FTIR) spectrometer was used as a high-resolution infrared Sun photometer in the solar trans-



Figure 1. Pictures from M'bour observation site when (top) clear and (bottom) dusty.

mission mode. PIRATE measurements were made for calibration in three locations under three atmospheric conditions (all dust and cloud-free). Dust-free (visible AOT < 0.3) measurements were made on 28 July 2005 in San Juan, Puerto Rico, 13 December 2005 in Santa Barbara, California, and 14 January 2006 in M'bour, Senegal (60 miles south of Dakar) at the Institute for Research and Development (IRD). Light dust (visible AOT \sim 0.5) measurements were made in San Juan on 25 July 2005 and M'bour on 15–16 January 2006. Heavy dust (visible AOT > 1) measurements were made in M'bour on 8–12 March 2006.

[6] The PIRATE equipment was setup within 20 feet of an AERONET sensor during the measurements in Santa Barbara and M'bour so that the AERONET's visible measurements of the dust AOT, size distribution, zenith angle and water vapor could be directly used for comparison. For Puerto Rico the closest AERONET sensor was in La Parguera, about 75 miles away from San Juan, so the AERONET AOT results are an approximation of the dust observed in San Juan. A summary of the experiment dates, conditions and locations is shown in Table 1. The AOT, water vapor and mean radius, r_m , are from AERONET while the ozone is from the Ozone Monitoring Instrument [Dobber *et al.*, 2008].

[7] The PIRATE equipment consists of the FTIR mounted on a motorized (Sun tracking) tripod, a pinhole camera above the FTIR to track the alignment of the FTIR relative to the Sun, a removable aperture in front of the FTIR to reduce the magnitude of the impinging solar spectral radiation, two blackbodies for calibration, a computer to control the FTIR and digitize its interferograms, and software to transform the interferograms into spectral irradiance. The FTIR is a Block model 100 LWIR with a 1" diameter entrance aperture, a $1.5^\circ \times 1.5^\circ$ field of view (FOV), 4 cm^{-1} spectral resolution and 4-Hz scan rate. Although the FTIR can measure spectra from 3 to $13 \mu\text{m}$, the signal-to-noise is best at the longwave

Table 1. Experiment Dates, Locations, Purpose, Visible AOT, Water Vapor, Ozone, and Mean Radius

Date	City	Location	Purpose	AOT (670 nm)	Water Vapor (mg/cm ²)	Ozone (DU)	r_m (μm)
25 July 2005	San Juan, Puerto Rico	Isla Verde Hotel	Data	0.4	3.9	280	0.1
28 July 2005	San Juan, Puerto Rico	Isla Verde Hotel	Calibration	0.15	3.9	280	0.1
13 December 2005	Santa Barbara, CA	UCSB	Calibration	0.1	1.2	275	0.1
14 January 2006	M'bour, Senegal	IRD	Calibration	0.1	2.4	285	0.1
15–16 January 2006	M'bour, Senegal	IRD	Data	0.5	2.2	245	0.2
8–12 March 2006	M'bour, Senegal	IRD	Data	1.1–2.5	1.1	260	0.2

end of this range (8–13 μm). The Orion Atlas tripod used has motorized control and 0.05° angular resolution in declination and right ascension. The pinhole camera has a 0.12" aperture and a 12" focal length and is mounted to the top of the FTIR. The FTIR spectral irradiance-limiting aperture is a 1" diameter aluminum disk painted black on the side facing the FTIR with a 0.3" diameter hole, making the through area about 9%. The aperture was necessary to limit the solar spectral irradiance to an acceptable range to prevent saturation of the FTIR detector. Figure 2 shows a picture of the PIRATE equipment and an author (the FTIR operator) setup next to the AERONET sensor on the roof of the IRD in M'bour.

[8] The IR AOT was measured in a solar transmission mode with the FTIR operating as an IR Sun photometer. The visible AOT, water vapor and zenith angle at the time of each FTIR measurement were taken from nearby AERONET sensors for reference. The FTIR recorded the direct and diffuse (within about 2°) solar spectral irradiance several times a day, and $\pm 5^\circ$ scans in declination across the solar disk were performed once daily to determine if any measurable signal resulted from scattering by dust in the IR (as opposed to attenuation) [Nakajima *et al.*, 1983; Dubovik *et al.*, 1995; Nakajima and Higurashi, 1997; Dubovik *et al.*, 1998, 2000, 2006].

[9] Figure 3 shows the measured normalized irradiance versus scan angle. This indicates that no scattering was observed during either heavy (10 March) or light (16 January) dust events since the full-width normalized spectral irradiance versus angle at 8.9 and 11.5 μm on both days was about 2°, which corresponds to the 1.5°FOV plus the 0.5° solar angle. On the basis of Mie calculations with indices of refraction from the Volz [1973] Saharan dust, Barbados, if scattering were present the signal should have been greater

at 8.9 μm than at 11.5 μm and we measured no such difference. The lack of measurable forward scattering in the IR is not surprising since the average dust mode radius is likely much smaller ($<1 \mu\text{m}$) than the measured wavelength ($>8 \mu\text{m}$). The difference in the irradiance for the 2 days at -0.5° and -1° scan angles indicates scans across slightly different regions of the FTIR detector. The asymmetry around 0° is due to variations in the FTIR responsivity with angle. For this reason, all subsequent measurements were made with the same solar alignment near 0° .

2.1. Data Collection Procedure

[10] The data collection procedure for each spectral irradiance measurement cycle is described below. Each cycle took about 10 min to complete. (1) Measure blackbody without aperture at 125°C, then without and with 0.3" aperture at 75°C. (2) Align FTIR to Sun using pinhole camera, then measure solar signals with 0.3" aperture. (3) Repeat procedure 1 in reverse order.

2.2. FTIR Calibration

[11] The FTIR was calibrated twice each measurement cycle using two portable blackbodies, one normally at 75°C and the other at 125°C. The 2" diameter blackbody surface was placed 2" in front of the 1" diameter FTIR entrance aperture for each measurement. The emissivity of the blackbodies is 0.97 ± 0.02 in the 8- to 13- μm band. No account of the nonunity emissivity was made in the irradiance computations since the controller sets the actual blackbody temperature slightly higher to make the average brightness temperature equal to the set temperature. We also did not factor in the irradiance reflected by the blackbody since even



Figure 2. Photograph of PIRATES equipment (background) setup near the Dakar AERONET sensor (foreground). The FTIR is on the tripod.

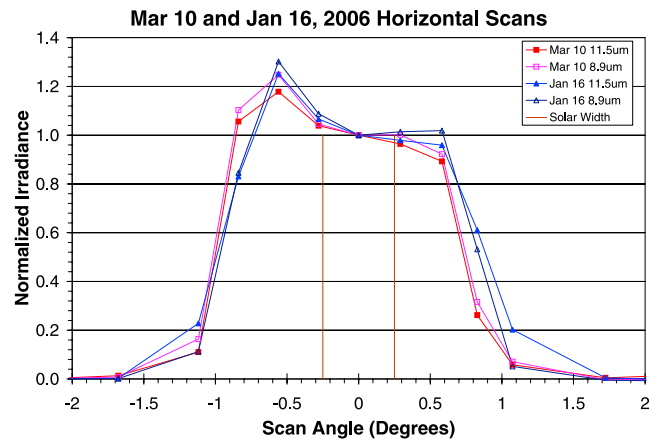


Figure 3. Normalized irradiance versus FTIR scan angle for two wavelengths on 16 January and 10 March 2006. No discernible signal is seen beyond 2° when dusty (10 March). The 0.5° width for the solar source is shown for reference.

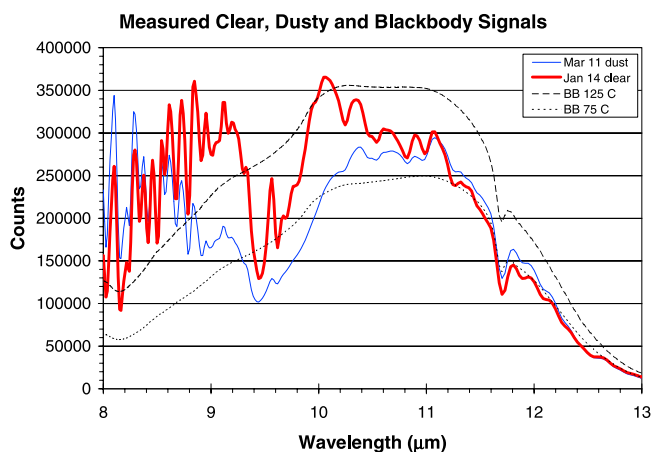


Figure 4. Measured blackbody (75°C and 125°C) and solar signals for 14 January (clear) and 11 March (dusty) in FTIR counts. The blackbody signals were measured without apertures, while the solar signals were with apertures.

at worst case the ratio of the $\sim 3\%$ reflected ambient (35°C) irradiance to the 97% emissive irradiance from the 75°C blackbody is less than 2%. To see the magnitudes of the blackbody signals in relation to the measured solar signals (in counts to show the measured magnitudes before conversion to irradiance), Figure 4 shows a plot of the two blackbody signals (no aperture) along with measured solar signals (with the aperture) from 14 January 2006 (clear) and 11 March 2006 (dusty). Ideally the solar signals should be between the two blackbody signals at all wavelengths since that would produce the lowest calibration error. Indeed, the two solar signals are within this range for most of the wavelengths, so the $11 \times$ attenuation of the aperture is about right. However, the solar signals are above the 125°C blackbody signal for wavelengths below about $9.3 \mu\text{m}$ on 14 January while the 11 March signal is below the 75°C blackbody signal in the area of the ozone band ($9.3\text{--}10 \mu\text{m}$).

[12] To determine how linear the FTIR is for the range of solar signals measured, data were taken for blackbody temperatures of 55°, 75°, 125° and 200°C. A measure of the FTIR counts versus calculated input spectral irradiance (from the blackbody temperature and Planck's function) for three wavelengths (8.1, 9 and $10 \mu\text{m}$) and three temperatures (75°, 125° and 200°C) is shown in Figure 5 (at $10 \mu\text{m}$ the 200°C point is not shown). The line for each wavelength is based on the slope computed from the 75°C and 125°C points, since those were the two temperatures normally used to characterize the FTIR response. The response is linear from 55°C to 125°C with a Pearson correlation coefficient, R^2 , of greater than 0.994 at all wavelengths from 8 to $13 \mu\text{m}$. However, it is obvious from the 8.1 and $9 \mu\text{m}$ data that the FTIR response is not linear for the higher (200°C) signal levels. Also shown, for comparison, are vertical bars indicating the combined range of solar signal counts from 14 January (clear) and 11 March (dusty) for all three wavelengths. The irradiances for these data points were set to cross the line connecting the 75°C and 125°C points.

[13] When the solar signals lie between or close to the 75° and 125°C blackbody signals, linear interpolation of the solar signal counts to irradiance using the 75° and 125°C black-

body data will have little error ($<3\%$). This is true for wavelengths from about 10 to $12 \mu\text{m}$. Below $9.3 \mu\text{m}$ for 14 January and below $8.8 \mu\text{m}$ for 11 March the measured solar signals exceed the blackbody signals for 125°C by as much as a factor of 3, while between 9.3 and $10 \mu\text{m}$ the solar signal for 11 March is as much as 35% less than the blackbody signal for 75°C. To assess the errors due to these excursions from the normal signal range and the FTIR nonlinearity, we computed what the FTIR counts should have been based on the 55°-to-75°C slope or the 125°-to-200°C slope, depending on whether the excursion was low or high, respectively. We then determined the AOT for the difference between the corrected and measured values and then for the high-excursion cases, for example, $8.1 \mu\text{m}$, determined the difference in the AOTs for the high and low signal levels at each wavelength. The AOT error from the FTIR nonlinearity is then the maximum of the low- and high-excursion AOTs. As shown in Figure 6, the AOT error is quite variable with wavelength, with peaks at 8.0, 8.2, 8.8, 11.7 and $12.5 \mu\text{m}$, but the FTIR nonlinearity AOT error is less than 0.2 from 8 to $13 \mu\text{m}$.

[14] To partially compensate for the FTIR nonlinearity we used an irradiance-fitting procedure (described below using SBDART and an adjustment to the aperture counts based on the 75°C blackbody measurement with the aperture), to make the measured dust-free irradiance equal to the computed SBDART irradiance (at all wavelengths). Thus we employed a unique correction term at each wavelength to linearize the FTIR response for the dust-free irradiance levels. We used the same adjustment for the dusty measurements. Consequently we estimate the AOT error for the FTIR nonlinearity (and nonunity blackbody emissivity) to be somewhat less than that shown in Figure 6.

[15] In Figure 4 the measured dusty counts (11 March) exceed the clear counts (14 January) below $8.4 \mu\text{m}$ owing to the lower water vapor during the dusty conditions. These differences in the atmospheric profiles between measurements on different days were calibrated out using SBDART

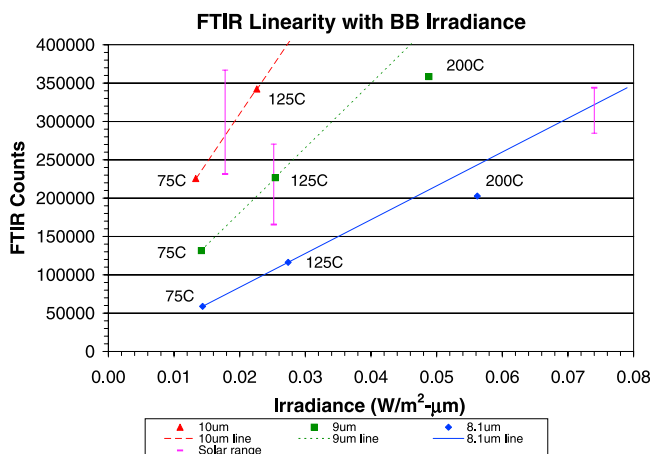


Figure 5. Plot of FTIR linearity at three wavelengths for 75°, 125°, and 200°C blackbody temperatures. The vertical lines show the range of counts from solar measurement with the aperture for 14 January and 11 March, with the irradiance for each wavelength set to span the 75°C- to -125°C counts-to-irradiance line.

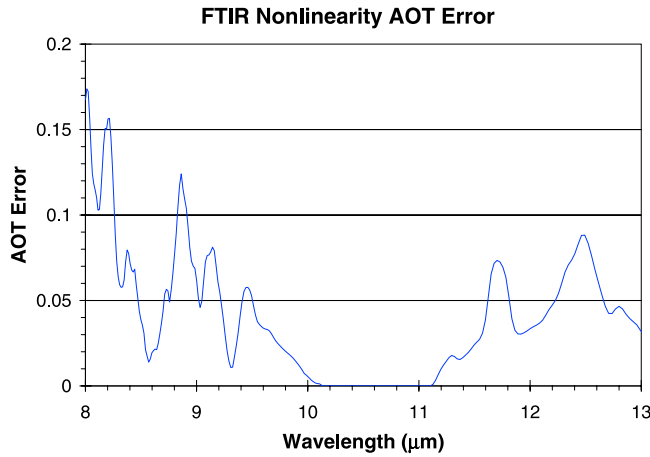


Figure 6. FTIR nonlinearity error based on solar signals from 14 January and 11 March. The AOT error is computed from the difference between the corrected counts and the measured counts. The corrected solar signal counts are computed when the solar signal is outside the 75° to 125°C range. In that case the correction factor is based on the 55° to 75°C slope for the low signals and the 125° to 200°C slope for the high signals, both relative to the 75° to 125°C slope.

spectral irradiance computation results [Ricchiuzzi *et al.*, 1998] (see section 3), a high-spectral resolution radiative transfer model that combines a correlated- k approximation together with the discrete ordinate technique [Yang *et al.*, 1999], along with dust-free measurements made in Santa Barbara and M'bour with similar water vapor and ozone levels to the dusty cases. Thus, although the measured counts for 14 January and 11 March appear to contradict each other at some wavelengths, when converted to irradiance and compared to SBDART models using measured atmospheric properties, the results are more consistent. The SBDART model has an accuracy of about 3% relative to line-by-line models.

3. Spectral Irradiance Calculations

[16] The solar spectral irradiance calculations require blackbody measurements, solar measurements, and instrument calibration using modeled clear-sky spectral irradiances. The forward computations of direct and diffuse downwelling solar spectral irradiances under dust-free conditions were made using SBDART. We used irradiance rather than radiance in our calculations because we knew the FTIR FOV and could account for the solid angle, in addition to being able to better account for the aperture emission.

[17] The spectral resolution, central wave numbers and FOV for SBDART were set to those of the FTIR, while the zenith angle and water vapor were set to those determined by AERONET, and the ozone was set to that determined by OMI. SBDART runs were performed for the 13 December 2005 measurements using a midlatitude winter [McClatchy *et al.*, 1972] temperature profile increased by 20°C at the surface (to match the actual temperatures), and for 14–16 January 2006 and 8–12 March 2006 using a tropical temperature profile increased by 10°C at the surface. The 13 December and 14 January SBDART runs were used for calibrating the response of the spectral irradiance calculations under dust-free conditions as described below. Owing

to the larger FTIR FOV (relative to the Sun's 0.5° disc), both direct and diffuse spectral irradiances were computed in the SBDART runs.

[18] All FTIR measurements (BB, aperture and solar) used an average of 50 interferograms for noise suppression. The interferograms were Fourier-transformed into spectra (counts versus wavelength) using triangular apodization, dc offset correction, phase shift correction and $2 \times$ zero filling. The before and after blackbody spectra (see section 2.1) at each temperature were averaged for noise reduction. Between five and ten measurements were made of the solar irradiance each observation day.

[19] The first task in computing the solar spectral irradiance is to compute the blackbody spectral irradiance projected into the FTIR using equation (1) (based on Planck's Law) for each temperature (where $1.5 \text{ deg} \times 1.5 \text{ deg}$ is the full FOV of the FTIR) assuming an emissivity of 1 and a wavelength dependence for the spectral irradiance, I . The constants h , c and k in equation (1) are Planck's constant, the speed of light and Boltzmann's constant, respectively, and λ is the wavelength.

$$I(T)_{BB} = \frac{(2hc)[2\pi(1 - \cos(1.5/2))](4/\pi)}{\lambda^5 (e^{\frac{hc}{\lambda T}} - 1)}. \quad (1)$$

The next task is to determine the spectral irradiance/counts slope, dI/dC , at each wavelength using equation (2) with no aperture using blackbody measurements at 75°C and 125°C.

$$\frac{dI}{dC_{open}} = \frac{I_{125C} - I_{75C}}{C_{125C} - C_{75C}}. \quad (2)$$

The third task is to determine the spectral irradiance offset, I_{off} , at each wavelength using equation (3) with no aperture using the blackbody measured counts at 75°C, C_{75C} , the computed spectral irradiance at 75°C, I_{75C} , and dI/dC . The irradiance offset primarily comes from internal emissions within the FTIR.

$$I_{off} = C_{75C} \frac{dI}{dC_{open}} - I_{75C}. \quad (3)$$

The solar spectral irradiance at each wavelength is determined using the terms above, the measured solar signal in counts, C_m , the blackbody signal at 75°C with the aperture, $C_{75C+aper}$, and the calculated aperture self emission counts, C_{aper} , as shown in equation (4). Since the FTIR self emission irradiance offset is contained within the I_{off} term, the only other thermally emitting object besides the Sun, atmosphere and aerosol is the aperture, and this emission is subtracted from the measured solar signal prior to conversion to irradiance in equation (4). The C_m multiplier in equation (4) (in the parentheses) represents the inverse of the transmission of the aperture with the aperture self emission subtracted.

$$I(\lambda) = \frac{dI}{dC_{open}} \left[C_m \left(\frac{C_{75C}}{C_{75C+aper} - C_{aper}} \right) - C_{aper} \right] + I_{off}. \quad (4)$$

The aperture irradiance, C_{aper} , is dependent on its temperature, but since its outer surface was reflective and we kept it in

the shade when not in use, its temperature was always close to ambient; this was verified periodically with a temperature probe on the surface of the aperture. The aperture's inner surface was painted black to minimize reflections of thermal sources from within the FTIR. We determined that the best method for computing the aperture irradiance signal, C_{aper} , was to measure the aperture with the 75°C blackbody behind it since this provided a stable source filling the aperture opening (we also tried viewing the cold sky but its irradiance was too variable). This measurement gives the $C_{75C+aper}$ term which equals the 75°C blackbody signal dimmed by the aperture and the aperture emission signal. The dimmed 75°C blackbody irradiance is always the same, so any changes in the $C_{75C+aper}$ term are due to aperture temperature changes (or changes in the FTIR but those are compensated for in the I_{off} and dI/dC terms in equations (3) and (4)). Thus we conclude that the $C_{aper}/C_{75C+aper}$ ratio is basically constant (approximately equal to 0.75), so by multiplying this ratio by a measured $C_{75C+aper}$ signal we can retrieve the corresponding C_{aper} signal as formulated in equation (5).

$$C_{aper} = C_{75C+aper} \left[\frac{C_{aper}}{C_{75C+aper}} \right]_{Cal}. \quad (5)$$

We determined the $C_{aper}/C_{75C+aper}$ ratios using two calibration days to tune the computed irradiance from equation (4) to match the corresponding spectral irradiance from SBDART. This way our calculations of the irradiance under dust free conditions match the computed SBDART irradiance, so any differences between the measured irradiance during noncalibration days and the corresponding SBDART irradiance is due to dust extinction. It turns out water vapor plays a significant role in the irradiance measurements, so to minimize errors from water vapor separate calibrations were used for each range of water vapor corresponding to our dust measurement conditions. Thus the 13 December 2005 calibration was used with the 8–12 March 2006 measurements since they both had water vapor column densities of about 1 g/cm², and the 14 January 2006 calibration was used with the 15–16 January 2006 measurements since both had water vapor column densities of around 2.3 g/cm².

[20] The $[C_{aper}]_{Cal}$ terms for the two clear calibration days were calculated using equation (9). This equation was obtained, as shown in the progression in equations (6)–(8), by starting with equation (4) and solving for C_{aper} with C_m set to the measured clear solar counts and I_C set to the computed clear irradiance from SBDART. Then we divided the computed C_{aper} by the measured $C_{75C+aper}$ to obtain the ratio used in equation (5). This ratio, though still approximately 0.75, now has dips at some wavelengths due to water vapor and ozone absorption; the dips are needed to get the measured irradiance to equal the SBDART radiance at all FTIR wavelengths. The Cal subscript in equations (5) and (9) refer to the fact that the C_{aper} value was obtained from a calibration measurement and calculation. Consequently the C_{aper} terms in equations (4), (5) and (9) all represent the same thing: the aperture self emission. As a sensitivity analysis, we calculated that a large 10°C change in the aperture temperature (were it not accounted for in the $C_{75C+aper}$ signal) would produce a difference in the solar signal of only about 10,000 counts, less than 3% of the typical solar

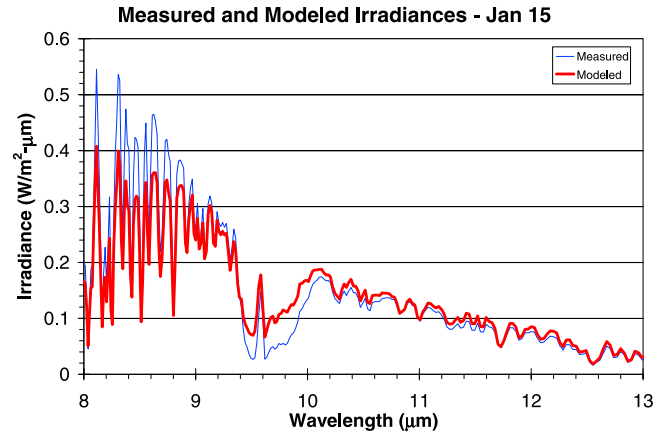


Figure 7. Measured and modeled irradiances for 15 January 2006 in Senegal.

signal with the aperture. This is insignificant compared to the other errors.

$$(C_{75C+aper} - C_{aper}) \left(\frac{I_C - I_{off}}{dI/dC_{open}} \right) = C_m C_{75C} - C_{aper} (C_{75C+aper} - C_{aper}), \quad (6)$$

$$(C_{75C+aper}) \left(\frac{I_C - I_{off}}{dI/dC_{open}} \right) - C_m C_{75C} = C_{aper} \left(\frac{I_C - I_{off}}{dI/dC_{open}} \right) - C_{aper} (C_{75C+aper} - C_{aper}), \quad (7)$$

$$\left[C_m C_{75C} - C_{75C+aper} \left(\frac{I_C - I_{off}}{dI/dC_{open}} \right) \right] + C_{aper} \left[\left(\frac{I_C - I_{off}}{dI/dC_{open}} \right) - C_{75C+aper} \right] + C_{aper}^2 = 0. \quad (8)$$

Equation (8) is a quadratic equation with variable C_{aper} which can be solved using the quadratic formula. Equation (9) shows the solution for C_{aper} , where C_{aper} has been given the name $C_{aperCal}$ because this equation is only used during clear calibrations.

$$C_{aperCal} = 0.5 \left(\left\{ \left[\frac{I_C - I_{off}}{dI/dC} - C_{75C+aper} \right]^2 - 4 \left[C_m C_{75C} - C_{75C+aper} \left(\frac{I_C - I_{off}}{dI/dC} \right) \right] \right\}^{0.5} - \left(\frac{I_C - I_{off}}{dI/dC} - C_{75C+aper} \right) \right). \quad (9)$$

4. Spectral Irradiance Results

[21] Plots for measured and modeled (dust-free) spectral irradiances for 15 January 2006 are shown in Figure 7. This is for medium dust conditions with visible AOT about 0.4 at 670 nm (from AERONET). The measured spectral irradiances are very close to the modeled spectral irradiances, so the dust on 15 January did not appear to have much

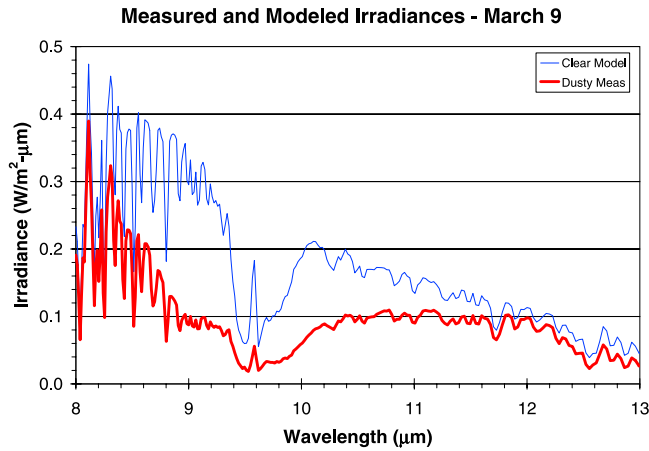


Figure 8. Measured (dusty) and modeled (clear) spectral irradiances for 9 March 2006 in Senegal.

attenuation in the infrared. Differences do exist owing to water vapor between 8 and 9 μm (strong water vapor lines exist in this part of the spectrum as opposed to the lower absorbing continuum in the 10- to 12- μm range) and ozone between 9.4 and 10 μm .

[22] A plot of the measured (dusty) spectral irradiance for one measurement on 9 March 2006 is shown in Figure 8 along with the corresponding dust-free modeled spectral irradiance. This is for heavy dust conditions with visible AOT about 2.5 at 670 nm and there appears to be considerable attenuation in the infrared. The differences between the attenuation on 15 January and 9 March are likely due to differences in the dust loading, size distributions and compositions.

5. Aerosol Optical Thickness

[23] The measured dusty irradiance, I_D , is a combination of the clear solar irradiance transmitted through the dust-free atmosphere and the emitted irradiance from the dust-free atmosphere, I_C , computed from SBDART, along with the extinction, $e^{-\tau_d/\cos(\theta)}$, and self emission from the dust, $(1-e^{-\tau_d/\cos(\theta)})I_E$. Equation (10) shows this relationship, assuming all of the dust is emitting at a constant temperature.

$$I_D = I_C e^{-\tau_d/\cos(\theta)} + (1 - e^{-\tau_d/\cos(\theta)}) I_E. \quad (10)$$

Under dust-free conditions, equation (10) shows that $I_D = I_C$. When dust is present, the dust infrared AOT, τ_d , is determined by inverting equation (10) as shown in equation (11) (where wavelength dependence is implied for each term),

$$\tau_d = (\ln(I_C - I_E) - \ln(I_D - I_E)) \cos(\theta), \quad (11)$$

where I_C and I_D are at the same solar zenith angle, θ , water vapor and date (to account for changes in the Earth-Sun distance). I_E is for a blackbody at 35°C at all wavelengths; 35°C was selected since the surface temperature for 9–11 March was about 40°C and the AIRS [Divakarla et al., 2006] air temperature at 925 mb was about 30°C. The dust emission

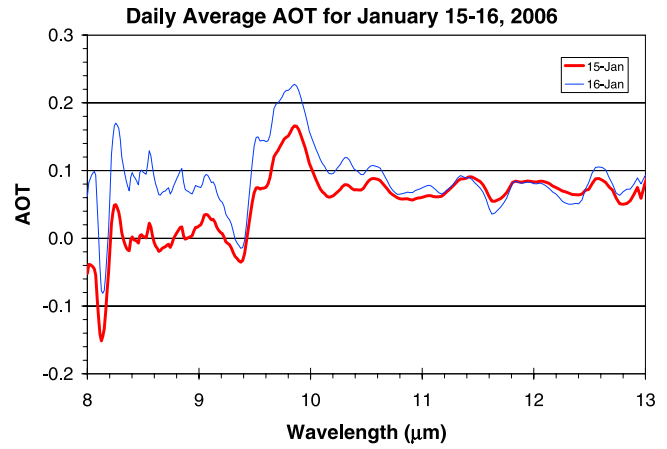


Figure 9. Daily average AOT for 15–16 January 2006 in Senegal.

irradiance relative to the direct solar irradiance is typically small (about 10%), though not negligible, especially at wavelengths where the AOT is higher. The AOT was determined using equation (10) from 8 to 13 μm with about 8 cm^{-1} (~ 80 nm) resolution after smoothing.

5.1. AOT Results

[24] Daily average IR AOT as a function of wavelength for 15–16 January 2008 are shown in Figure 9. These are for “medium” dust conditions with visible AOT around 0.4. The dip at 9.3 μm is due to the ozone transition and the dip at 8.14 μm is likely due to differences in the water vapor between 15–16 January in M’bour and the 13 December 2005 calibration measurements in Santa Barbara. Although the AOT signal-to-noise for this dust event is close to or less than 1:1 at most of the wavelengths (on the basis of the AOT error in section 5.2), in the vicinity of 9.8 μm the computed IR AOT is greater than the AOT error. The ratio of the 670 nm AOT to the 9.8 μm AOT (visible/IR) is 0.5/0.2 = 2.5.

[25] The daily average IR AOT spectra for 8–12 March 2006 are shown in Figure 10. These are for “heavy” dust conditions with visible AOT > 1 at 670 nm. The main features in these AOT spectra are a principal AOT peak in the 9- to

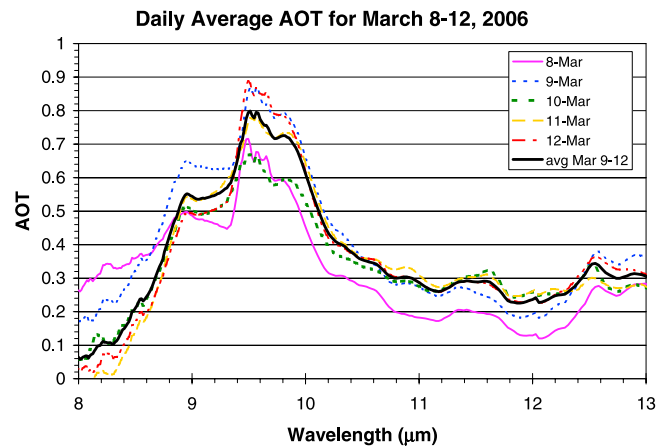


Figure 10. Daily average AOT for 8–12 March 2006 in Senegal.

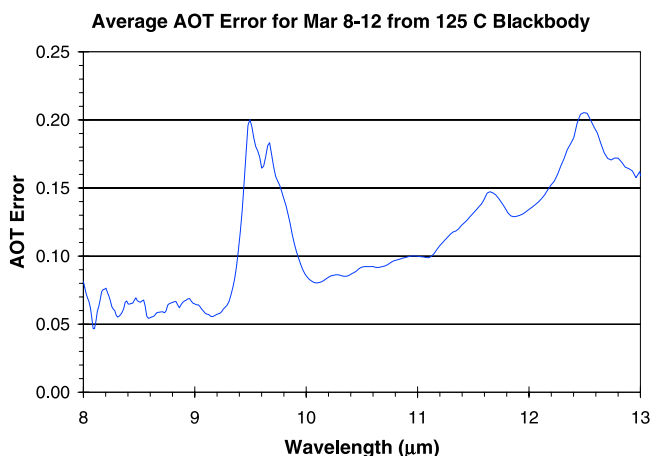


Figure 11. Average AOT error versus wavelength for 8–12 March 2008 based on the daily standard deviation of AOT retrievals using the 125°C blackbody signal instead of the solar signal (C_m in equation (4)).

10- μm range and a secondary rise above 12 μm (even after subtracting off residual water vapor OT above 12 μm). Both of these AOT features, as well as the general shape of the AOT spectra with decreases at 8 and 12 μm , are consistent with radiance measurements made by Turner [2008] for the March 2006 dust plume and the brightness temperature difference measurements (clear minus dusty) from Highwood *et al.* [2003] for a 2003 Saharan dust plume measured from above the dust layer. The ratio of the 670 nm AOT to the 9.8 μm AOT (visible/IR) is $2.1/0.7 = 3.0$. This differs from the results of Turner [2008] where through radiance measurements of the March 2006 dust storm in Niamey, Niger, he found the ratio of the 1.02 μm AOT to the 11.0 μm AOT (NIR/IR) is 2.2, though the size distribution in Niamey was a little larger than in Dakar so this could have lowered the ratio. It also differs from the results of DeSouza-Machado *et al.* [2006], who found the 550 nm AOT from MODIS and the 11 μm AOT from AIRS to be related by $\text{AOT}(\text{VIS}) = \text{AOT}(\text{IR}) \times 0.425 - 0.084$ for Saharan dust over the Mediterranean Sea. However, Pierangelo *et al.* [2004] found for Saharan dust over the North Atlantic the relationship between the MODIS AOT at 550 nm and the AIRS AOT at 10 μm to have the ratio of $\text{AOT}(0.55 \mu\text{m})/\text{AOT}(10 \mu\text{m}) = 3.2$ which is close to what we measured. Thus there is some discrepancy between the visible to IR AOT ratios for dust depending on when, where and how the AOTs were measured. Pierangelo *et al.* [2004] found the visible to IR AOT ratio increases with distance from the source region; presumably this is due to the loss of larger dust particles with time and distance.

[26] The 8–12 March IR AOT curves have much broader peaks in the 9- to 10- μm range than the 15–16 January AOT. This difference could simply be due to the greater AOT in March, or it could be due to more subtle differences in the dust properties such as the presence of certain minerals or the dust size distribution. We are not sure if the differences in the visible/IR AOT ratios for January and March are significant, the former having low signal-to-noise. It is interesting, though, that AERONET's Angstrom exponent was lower for 15–16 January than for 8–12 March, making the computed

dust size distribution in January slightly larger than in March. This supports the idea that as the dust size distribution goes up, the IR AOT should go up and the visible/IR AOT ratio should go down, which is consistent with our results above.

5.2. AOT Error Analysis

[27] To compute the AOT error in our measurements each day, for each measurement cycle we substituted one of the 125°C BB measurements (in counts) for the solar signal (C_m in equation (4)), to factor in the slope, offset and aperture effects, then computed the irradiance standard deviation of these 125°C signals each day, then added this standard deviation irradiance to the average irradiance for that day, then computed the AOT for the average irradiance plus standard deviation, and finally subtracted this AOT from the AOT based only on the average irradiance to yield the AOT standard deviation for that day. The AOT error was computed as the average AOT standard deviation for the 5 days. The average error computed in this manner is shown in Figure 11. The error is lowest at 8.1–9.3 μm and 10–11 μm , and highest in the ozone band (9.4–10 μm) and above 12 μm owing to reduced FTIR sensitivity. When this AOT error is combined with the FTIR nonlinearity AOT error (Figure 6) using the root-sum-square method (since the errors are independent), the total AOT error for our measurements is found and shown in Figure 12. The total AOT error is always below 0.22 and the mean total error from 8 to 13 μm is 0.12.

5.3. Comparisons With AERONET

[28] The visible AOT (courtesy of D. Tanre) was measured by an AERONET (Cimel) Sun photometer next to the PIRATE equipment. Figure 13 shows a time series plot of the daily average AOT at 10 μm along with the daily average AOT at 670 nm from AERONET [Holben *et al.*, 1998] for 8–12 March. The vertical error bars for each point indicate \pm the standard deviation of the AOT each day at each wavelength. The correlation between the IR (10 μm) and visible AOTs

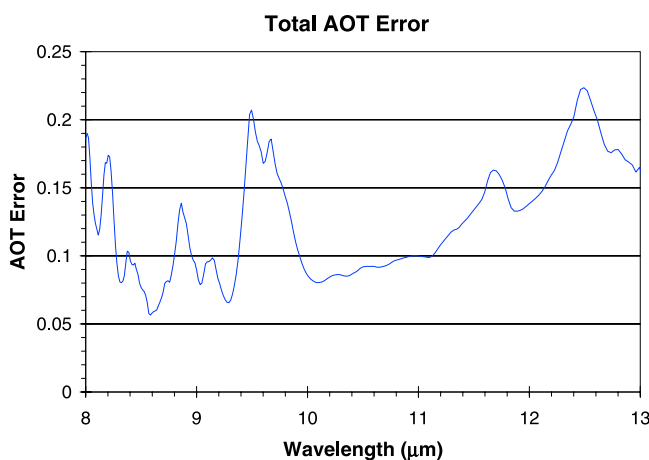


Figure 12. Total AOT error versus wavelength for 8–12 March 2008 based on the root-sum-square of the daily standard deviation of AOT retrievals for the 125°C blackbody signal (Figure 11) and the FTIR nonlinearity AOT error (Figure 6).

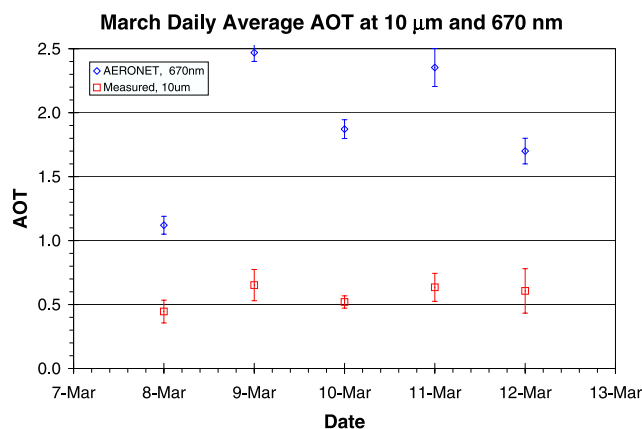


Figure 13. Time series of AOTs at 670 nm (from AERONET) and 10 μm (from our IR measurements) for 8–12 March 2006. The error bars represent the standard deviation (\pm) of the daily AOT.

for these dates is 0.98. Conversely the correlation for 15–16 January 2006 was close to 0. This low correlation is likely due to the low AOT (the IR AOT for 15–16 January was about equal to our detection limit of about 0.10; see section 5.2) and the fact that the comparison is for only two points, but it is possibly also due to the dust composition (mineral types and size distributions) and differences between assumed and actual atmospheric profiles.

[29] The average AERONET number size distribution for 9–11 March 2006 is shown in Figure 14. The data have three modes: 0.05 μm , 0.5 μm and 1.7 μm . A trimodal lognormal size distribution is also shown in Figure 14, where the geometric standard deviation, σ , is shown for each mode. For radii from 0.05 to 5 μm the sum of the lognormal curves closely matches the AERONET data. The root mean square (RMS) radius is 0.11 μm , the mean radius is 0.2 μm , and the effective radius is 1.3 μm .

5.4. Comparisons With Dust Models

[30] In this section we show comparisons between the measured spectral AOT and the computed AOTs for two predefined dust models. The modeled AOTs were derived using Mie calculations with indices of refraction from the Volz [1973] Saharan dust: Barbados and the Fouquart *et al.* [1987b] dust (only from 7 to 13 μm). To match the average measured AOT for 9–11 March the modeled AOT is set equal to 2.25 at 550 nm. The measured AOTs are from AERONET at 440, 670, 870 and 1020 nm, and our IR AOTs are at 15 wavelengths. First we looked at the Volz model using the trimodal AERONET size distribution. Figure 15 shows the computed AOT along with the measure AOTs. The Volz AOT does not match the average measured AOT for 9–11 March 2008 in both the visible and infrared wavelength ranges very well. One reason for this discrepancy is likely owing to AERONET's underreporting of the large particle AOT (the steep-sloped visible-NIR AOT for the Volz model in Figure 15 is due to the high concentration of small aerosols).

[31] To see if slightly larger size distributions improved the fit between the computed and measured AOTs we used single-mode lognormal size distributions with a standard deviation of 2 in our Mie calculations. This time we computed the AOT for both reference mixtures (Volz and Fouquart). The

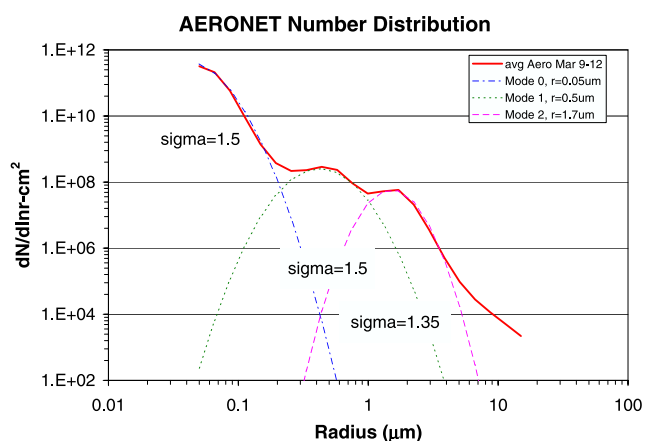


Figure 14. Average AERONET number size distribution for 9–12 March 2006.

comparisons show that the measured AOTs best match the modeled Volz AOT when the mode radius is 0.25 μm and the Fouquart AOT when the mode radius is 0.30 μm . Figure 16 shows these modeled AOTs along with the measured AOT. The modeled mode radii are slightly larger than the AERONET mean radius (0.2 μm) and the standard deviation of 2 is larger than the standard deviations of the trimodal distribution (1.3 to 1.7). The larger size distribution for the Volz model drastically changes the shape of the AOT in the visible to NIR. Whereas with the trimodal model the AOT decreased rapidly with wavelength, with the single-mode distribution the AOT slightly increases with wavelength. It is hard to say which fit is better in the visible to NIR. The Volz AOT with the single-mode distribution appears to better match the measured AOT between 9 and 10 μm than with the trimodal distribution, but the single-mode AOT is too high between 10 and 11 μm . The Fouquart AOT provides a better match to the measured AOT from 8 to 12 μm than the Volz AOT, but the lack of visible data for Fouquart makes it impossible to fully compare the two. Neither model shows a rise in the AOT above 12 μm , as the measured AOT does. The

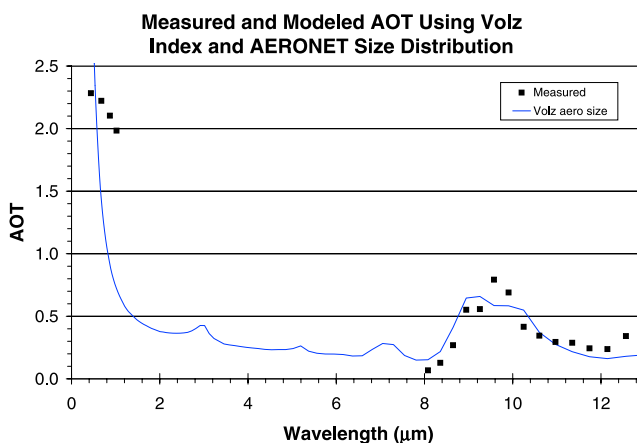


Figure 15. Modeled AOT using indices of refraction from Volz with AERONET size distribution (trimodal), and the measured AOT (squares) in the visible (from AERONET) and IR (from PIRATES).

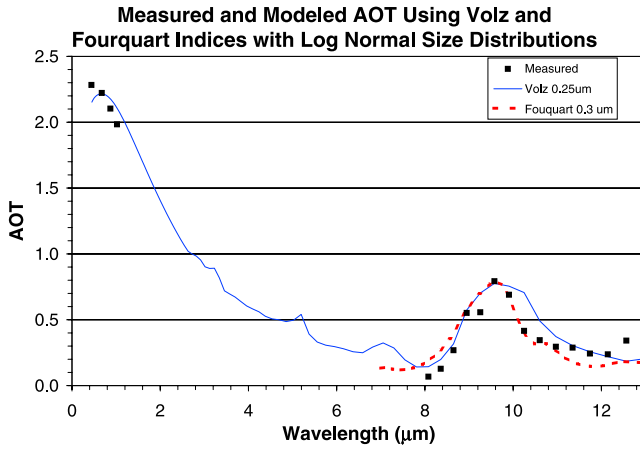


Figure 16. Measured (squares) and modeled AOTs using indices of refraction from Volz and Fouquart with lognormal size distributions of mode radii 0.25 and 0.3 μm , respectively, and $\sigma = 2$.

reason for this discrepancy is likely owing to the relative lack of quartz in the Volz and Fouquart samples.

6. Dust IR Forcing

[32] The dust IR forcing (W/m^2) at the surface can be calculated using the difference between the dusty and clear irradiances by determining the integral of the difference versus wavelength as shown in equation (12)

$$F_{\text{IR, Surface}} = \int_8^{13} (I_D - I_C) d\lambda = \sum_8^{13} (I_D - I_C) \Delta\lambda. \quad (12)$$

A plot of the difference between the dusty and clear irradiances from Figure 8 (from 9 March) is shown in Figure 17. This curve shows the regions of greater (8–9.3 μm) and lower (11–13 μm) IR forcing. There is also a dip from 9.4 to 9.8 μm due to stratospheric ozone. The integral of this curve gives the direct IR surface forcing to be -0.43 W/m^2 . This IR forcing cools the surface by blocking the downwelling solar flux and warms the atmosphere since the dust is mainly absorbing. This is not the same thing as the modeled results from Yoshioka *et al.* [2007], who found the average IR surface forcing from dust over the tropical Atlantic Ocean to be $+3 \text{ W/m}^2$ because their model factors in the downwelling IR flux emitted by the dust to warm the surface. Our measured forcing of -0.43 W/m^2 is not large when compared to the total solar cloudless downwelling surface flux ($\sim 970 \text{ W/m}^2$) [Seinfeld and Pandis, 1998], but the March dust plume blocked about half of the IR light from the Sun in the 8- to 13- μm part of the IR, and its forcing magnitude is equal to the annual average total direct aerosol forcing [Forster *et al.*, 2007], so for large dust plumes the direct IR surface forcing is not negligible.

7. Conclusions

[33] The results from the PIRATES experiment found that we were able to measure the IR AOT of dust plumes using an

FTIR in a solar occultation mode similar to AERONET, and the measured AOT from an ensemble of mineral aerosols of various sizes, shapes, orientations and mineral composition basically matches the data from Highwood and the AOT spectra computed using Mie calculations and the mineral indices of Volz and Fouquart with trimodal and single-mode size distributions, though the matches are not perfect, especially in the visible for Volz. The Volz and Fouquart models' AOTs lack some of the spectral structure seen in our measurements, most noticeably the lack of an AOT rise above 12 μm .

[34] One of the main conclusions we reached while doing this work is that mineral dust is normally transparent in the IR and the IR AOT is difficult to measure. This is based on the fact that we tried to measure a few dust plumes (two in Puerto Rico and one in Senegal) that were visible to the eye and had visible AOT > 0.3 yet were almost completely transparent in the IR. It is hard to allocate the cause for this as it could be due to the dust size, dust composition, atmospheric water vapor and temperature profiles, and/or detection limits in our equipment.

[35] For the 8–12 March dust plume we found the measured IR AOT peak at 9.5 μm is about 30% of the AOT at 670 nm. Thus for an assumed IR AOT error of 0.12, the 670 nm AOT must exceed about 0.36 and the size distribution must be moderately large in order for the IR AOT to be measurable with PIRATES. This is supported by the fact that we did not measure IR extinction for a dust plume in Puerto Rico when the AOT at 670 nm was 0.4 (the size distribution was very small), while we barely measured IR extinction for a dust plume in Senegal when the AOT at 670 nm was 0.5 (with a larger size distribution), and we easily measured IR extinction for a dust plume in Senegal when the AOT at 670 nm was over 1. We conclude that for a dust plume to have any measureable surface and atmospheric IR forcing impacts, the IR AOT must be at least 0.2. Since the visible/IR AOT ratio is approximately 2.5 to 3, the visible AOT must be at least 0.5, the dust size distribution must be relatively large and/or the dust composition must contain IR absorbing minerals in order to meet this requirement.

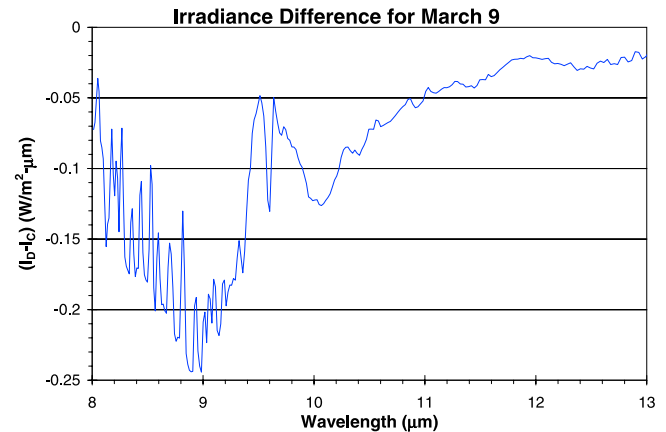


Figure 17. Irradiance difference ($I_D - I_C$) versus wavelength for the data from Figure 8. This curve shows the regions of greater (8–9.3 μm) and lower (11–13 μm) IR forcing. There is also a dip from 9.4 to 9.8 μm due to stratospheric ozone. The integral of this curve gives the total IR surface forcing due to dust in the 8- to 13- μm band to be -0.43 W/m^2 .

[36] Future work in this field should involve more IR (multispectral or hyperspectral) observations of dust from ground-based and space-based sensors to get better statistics on the correlation between the IR AOT and the visible AOT as well as better assessment of the variability in the IR AOT spectra from mineral dust. This could improve the formulation of models using IR dust radiative properties to determine mineral aerosols' role in affecting climate. Additionally, we plan to work on deciphering the mineralogy in the March 2006 dust plume on the basis of the visible and IR AOT spectra presented in this paper.

[37] **Acknowledgments.** This work was conducted under NASA contract NNG04GL20G. We wish to thank the Institute of Research and Development in M'bour, Senegal, and Tamsir Diop, Aboubacry Diallo, Thierno Ndiaye, and Barama Sow for their generous hospitality and support of our work, as well as Bernadette Chatenet of the Laboratoire Interuniversitaire des Systemes Atmospheriques and Didier Tanre of Laboratoire d'Optique Atmospherique, Université des Sciences et Technologies de Lille, CNRS, for their helpful support and facilitation of our work in Senegal. All the people we worked with in Africa were wonderful. We also thank Brent Holben and NASA GSFC for the use of their AERONET data. We thank the staff of the Holiday Inn, Isla Verde San Juan, Puerto Rico, for permitting measurements to be made at their hotel. We thank Pete Petersen and Claire Salustro of ICES for their help in processing the AERONET data. Finally, we thank the reviewers of this paper for their helpful comments and suggestions.

References

- Ackerman, S. A. (1997), Remote sensing aerosols using satellite infrared observations, *J. Geophys. Res.*, **102**(D14), 17,069–17,079, doi:10.1029/96JD03066.
- Ackerman, S. A., and H. Chung (1992), Radiative effects of airborne dust on regional energy budgets at the top of the atmosphere, *J. Appl. Meteorol.*, **31**, 223–236.
- Agassi, E., A. Ronen, N. Shiloah, and E. Hirsch (2006), Discrimination between natural dense dust clouds with IR spectral measurements, *Int. J. High Speed Electron. Syst.*, **18**(3), 647–660.
- Balkanski, Y., et al. (2006), Reevaluation of mineral aerosol radiative forcings suggests a better agreement with satellite and AERONET data, *Atmos. Chem. Phys. Discuss.*, **6**, 8383–8419.
- Claquin, T., et al. (1998), Uncertainties in assessing radiative forcing by mineral dust, *Tellus, Ser. B*, **50**(5), 491–505, doi:10.1034/j.1600-0889.1998.t01-2-00007.x.
- DeSouza-Machado, S. G., L. L. H. Strow, S. E. Hannon, and H. E. Motteler (2006), Infrared dust spectral signatures from AIRS, *Geophys. Res. Lett.*, **33**, L03801, doi:10.1029/2005GL024364.
- Divakarla, M., C. D. Barnet, M. D. Goldberg, L. M. McMillin, E. Maddy, and L. Z. W. Wolf (2006), Validation of AIRS temperature and water vapor retrievals with matched radiosonde measurements and forecasts, *J. Geophys. Res.*, **111**, D09S15, doi:10.1029/2005JD006116.
- Dobber, M., Q. Kleipool, R. Dirksen, P. Levelt, G. Jaross, S. Taylor, T. Kelly, L. Flynn, G. Leppelmeier, and N. Rozemeijer (2008), Validation of ozone monitoring instrument level 1b data products, *J. Geophys. Res.*, **113**, D15S06, doi:10.1029/2007JD008665.
- Dubovik, O. V., et al. (1995), Improved technique for data inversion: Optical sizing of multicomponent aerosols, *Appl. Opt.*, **34**(36), 8422–8436, doi:10.1364/AO.34.008422.
- Dubovik, O., B. N. Holben, Y. J. Kaufman, M. Yamasoe, A. Smirnov, D. Tanré, and I. Slutsker (1998), Single-scattering albedo of smoke retrieved from the sky radiance and solar transmittance measured from ground, *J. Geophys. Res.*, **103**(D24), 31,903–31,923, doi:10.1029/98JD02276.
- Dubovik, O., A. Smirnov, B. N. Holben, M. D. King, Y. J. Kaufman, T. F. Eck, and I. Slutsker (2000), Accuracy assessments of aerosol optical properties retrieved from Aerosol Robotic Network (AERONET) Sun and sky radiance measurements, *J. Geophys. Res.*, **105**(D8), 9791–9806, doi:10.1029/2000JD900040.
- Dubovik, O., et al. (2006), Application of spheroid models to account for aerosol particle nonsphericity in remote sensing of desert dust, *J. Geophys. Res.*, **111**, D11208, doi:10.1029/2005JD006619.
- Formenti, P., W. Elbert, W. Maenhaut, J. Haywood, and M. O. Andreae (2003), Chemical composition of mineral dust aerosol during the Saharan Dust Experiment (SHADE) airborne campaign in the Cape Verde region, September 2000, *J. Geophys. Res.*, **108**(D18), 8576, doi:10.1029/2002JD002648.
- Forster, P., et al. (2007), Changes in atmospheric constituents and in radiative forcing, in *Climate Change 2007: The Physical Science Basis. Contribution of Working Group I to the Fourth Assessment Report of the Intergovernmental Panel on Climate Change*, edited by S. Solomon et al., pp. 129–234, Cambridge Univ. Press, Cambridge, U. K.
- Fouquart, Y., et al. (1987a), Observations of Saharan aerosols: Results of ECLATS field experiment. Part 1: Optical thicknesses and aerosol size distributions, *J. Clim. Appl. Meteorol.*, **26**, 28–37, doi:10.1175/1520-0450(1987)026<0028:OOSARO>2.0.CO;2.
- Fouquart, Y., et al. (1987b), Observations of Saharan aerosols: Results of ECLATS field experiment. Part II: Broadband radiative characteristics of the aerosols and vertical radiative flux divergence, *J. Clim. Appl. Meteorol.*, **26**, 38–52, doi:10.1175/1520-0450(1987)026<0038:OOSARO>2.0.CO;2.
- Fraser, R. S. (1976), Satellite measurement of mass of Sahara dust in the atmosphere, *Appl. Opt.*, **15**(10), 2471–2479, doi:10.1364/AO.15.002471.
- Gao, Y., and J. R. Anderson (2001), Characteristics of Chinese aerosols determined by individual-particle analysis, *J. Geophys. Res.*, **106**(D16), 18,037–18,045, doi:10.1029/2000JD900725.
- Gasso, S., et al. (2000), Influence of humidity on the aerosol scattering coefficient and its effect on the upwelling radiance during ACE-2, *Tellus, Ser. B*, **52**(2), 546–567, doi:10.1034/j.1600-0889.2000.00055.x.
- Glaccum, R. A., and J. M. Prospero (1980), Saharan aerosols over the tropical North Atlantic—Mineralogy, *Mar. Geol.*, **37**, 295–321, doi:10.1016/0025-3227(80)90107-3.
- Goloub, P., et al. (1999), Validation of the first algorithm applied for deriving the aerosol properties over the ocean using the POLDER/ADEOS measurements, *IEEE Trans. Geosci. Remote Sens.*, **37**(3), 1586–1596, doi:10.1109/36.763270.
- Guelle, W., et al. (2000), Modeling the atmospheric distribution of mineral aerosol: Comparison with ground measurements and satellite observations for yearly and synoptic timescales over the North Atlantic, *J. Geophys. Res.*, **105**(D2), 1997–2012, doi:10.1029/1999JD901084.
- Haywood, J. M., et al. (2001), Optical properties and direct radiative effect of Saharan dust: A case study of two Saharan dust outbreaks using aircraft data, *J. Geophys. Res.*, **106**(D16), 18,417–18,430, doi:10.1029/2000JD900319.
- Highwood, E. J., J. M. Haywood, M. D. Silverstone, S. M. Newman, and J. P. Taylor (2003), Radiative properties and direct effect of Saharan dust measured by the C-130 aircraft during Saharan Dust Experiment (SHADE): 2. Terrestrial spectrum, *J. Geophys. Res.*, **108**(D18), 8578, doi:10.1029/2002JD002552.
- Holben, B. N., et al. (1998), AERONET—A federated instrument network and data archive for aerosol characterization, *Remote Sens. Environ.*, **66**(1), 1–16, doi:10.1016/S0034-4257(98)00031-5.
- Hsu, N. C., J. R. Herman, and C. Weaver (2000), Determination of radiative forcing of Saharan dust using combined TOMS and ERBE data, *J. Geophys. Res.*, **105**(D16), 20,649–20,661, doi:10.1029/2000JD900150.
- Jankowiak, I., and D. Tanre (1992), Satellite climatology of Saharan dust outbreaks: Method and preliminary results, *J. Clim.*, **5**, 646–656, doi:10.1175/1520-0442(1992)005<0646:SCOSDO>2.0.CO;2.
- Kaufman, Y. J. (1987), Satellite sensing of aerosol absorption, *J. Geophys. Res.*, **92**(D4), 4307–4317, doi:10.1029/JD092JD04p04307.
- Kaufman, Y. J., D. Tanré, H. R. Gordon, T. Nakajima, J. Lenoble, R. Frouin, H. Grassl, B. M. Herman, M. D. King, and P. M. Teillet (1997), Passive remote sensing of tropospheric aerosol and atmospheric correction for the aerosol effect, *J. Geophys. Res.*, **102**(D14), 16,815–16,830.
- Kaufman, Y. J., B. N. Holben, D. Tanré, I. Slutsker, A. Smirnov, and T. F. Eck (2000), Will aerosol measurements from Terra and Aqua polar orbiting satellites represent the daily aerosol abundance and properties?, *Geophys. Res. Lett.*, **27**(23), 3861–3864, doi:10.1029/2000GL011968.
- King, M. D., et al. (1999), Remote sensing of tropospheric aerosols from space: past, present, and future, *Bull. Am. Meteorol. Soc.*, **80**(11), 2229–2259, doi:10.1175/1520-0477(1999)080<2229:RSOTAF>2.0.CO;2.
- Legrand, M., et al. (1988), Satellite detection of Saharan dust: Optimized imaging during nighttime, *J. Clim.*, **1**, 256–264, doi:10.1175/1520-0442(1988)001<0256:SDOSDO>2.0.CO;2.
- Legrand, M., et al. (1989), The potential of infrared satellite data for the retrieval of Saharan-dust optical depth over Africa, *J. Appl. Meteorol.*, **28**, 309–319.
- Li, Z. (1995), Intercomparison between two satellite-based products of net surface shortwave radiation, *J. Geophys. Res.*, **100**(D2), 3221–3232, doi:10.1029/94JD02687.
- Li, Z. (1998), Influence of absorbing aerosols on the inference of solar surface radiation budget and cloud absorption, *J. Clim.*, **11**, 5–17, doi:10.1175/1520-0442(1998)011<0005:IOAAOT>2.0.CO;2.
- Liao, H., and J. H. Seinfeld (1998), Radiative forcing by mineral dust aerosols: sensitivity to key variables, *J. Geophys. Res.*, **103**(D24), 31,637–31,645, doi:10.1029/1998JD200036.

- Marticorena, B., G. Bergametti, B. Aumont, Y. Callot, C. N'Doumé, and M. Legrand (1997), Modeling the atmospheric dust cycle: 2. Simulation of Saharan dust sources, *J. Geophys. Res.*, **102**(D4), 4387–4404, doi:10.1029/96JD02964.
- McClatchy, R. A., et al. (1972), *Optical Properties of the Atmosphere, AFCRL-72-0497*, 80 pp., Air Force Cambridge Res. Lab., Bedford, Mass.
- Mishchenko, M. I., and L. D. Travis (1997), Satellite retrieval of aerosol properties over the ocean using polarization as well as intensity of reflected sunlight, *J. Geophys. Res.*, **102**(D14), 16,989–17,013, doi:10.1029/96JD02425.
- Mishchenko, M. I., L. D. Travis, R. A. Kahn, and R. A. West (1997), Modeling phase functions for dustlike tropospheric aerosols using a shape mixture of randomly oriented polydisperse spheroids, *J. Geophys. Res.*, **102**(D14), 16,831–16,847, doi:10.1029/96JD02110.
- Moorthy, K. K., A. Saha, B. S. N. Prasad, K. Niranjana, D. Jhurry, and P. S. Pillai (2001), Aerosol optical depths over peninsular India and adjoining oceans during the INDOEX campaigns: Spatial, temporal, and spectral characteristics, *J. Geophys. Res.*, **106**(D22), 28,539–28,554, doi:10.1029/2001JD00169.
- Nakajima, T., and A. Higurashi (1997), AVHRR remote sensing of aerosol optical properties in the Persian Gulf region, summer 1991, *J. Geophys. Res.*, **102**(D14), 16,935–16,946, doi:10.1029/96JD01935.
- Nakajima, T., et al. (1983), Retrieval of the optical properties of aerosols from aureole and extinction data, *Appl. Opt.*, **22**(19), 2951–2959, doi:10.1364/AO.22.002951.
- Perlitz, J., I. Tegen, and R. L. Miller (2001), Interactive soil dust aerosol model in the GISS GCM: 1. Sensitivity of the soil dust cycle to radiative properties of soil dust aerosols, *J. Geophys. Res.*, **106**(D16), 18,167–18,192, doi:10.1029/2000JD000668.
- Petit, R. H., M. Legrand, I. Jankowiak, J. Molinié, C. Asselin de Beauville, G. Marion, and J.-L. Mansot (2005), Transport of Saharan dust over the Caribbean Islands: Study of an event, *J. Geophys. Res.*, **110**, D18S09, doi:10.1029/2004JD004748.
- Pierangelo, C., et al. (2004), Dust altitude and infrared optical depth from AIRS, *Atmos. Chem. Phys.*, **4**, 1813–1822.
- Prospero, J. M., P. Ginoux, O. Torres, S. E. Nicholson, and T. E. Gill (2002), Environmental characterization of global sources of atmospheric soil dust identified with the NIMBUS 7 Total Ozone Mapping Spectrometer (TOMS) absorbing aerosol product, *Rev. Geophys.*, **40**(1), 1002, doi:10.1029/2000RG000095.
- Ricchiazzi, P., et al. (1998), SBDART: A research and teaching software tool for plane-parallel radiative transfer in the Earth's atmosphere, *Bull. Am. Meteorol. Soc.*, **79**(10), 2101–2114, doi:10.1175/1520-0477(1998)079<2101:SARATS>2.0.CO;2.
- Schmid, B., et al. (2000), Clear-sky closure studies of lower tropospheric aerosol and water vapor during ACE-2 using airborne sunphotometer, airborne in-situ, space-borne, and ground-based measurements, *Tellus, Ser. B*, **52**(2), 568–593, doi:10.1034/j.1600-0889.2000.00009.x.
- Seinfeld, J. H., and S. N. Pandis (1998), *Atmospheric Chemistry and Physics: From Air Pollution to Climate Change*, 1326 pp., John Wiley, Hoboken, N. J.
- Slingo, A., et al. (2006), Observations of the impact of a major Saharan dust storm on the atmospheric radiation balance, *Geophys. Res. Lett.*, **33**, L24817, doi:10.1029/2006GL027869.
- Sokolik, I. N. (2002), The spectral radiative signature of wind-blown mineral dust: Implications for remote sensing in the thermal IR region, *Geophys. Res. Lett.*, **29**(24), 2154, doi:10.1029/2002GL015910.
- Tanre, D., and M. Legrand (1991), On the satellite retrieval of Saharan dust optical thickness over land: two different approaches, *J. Geophys. Res.*, **96**(D3), 5221–5227, doi:10.1029/90JD02607.
- Tanre, D., P. Y. Deschamps, C. Devaux, and M. Herman (1988), Estimation of Saharan aerosol optical thickness from blurring effects in Thematic Mapper data, *J. Geophys. Res.*, **93**(D12), 15,955–15,964, doi:10.1029/JD093iD12p15955.
- Tegen, I., and I. Fung (1994), Modeling of mineral dust in the atmosphere: Sources, transport and optical thickness, *J. Geophys. Res.*, **99**(D11), 22,897–22,914, doi:10.1029/94JD01928.
- Torricella, F., E. Cattani, M. Cervino, R. Guzzi, and C. Levoni (1999), Retrieval of aerosol properties over the ocean using Global Ozone Monitoring Experiment measurements: Method and applications to test cases, *J. Geophys. Res.*, **104**(D10), 12,085–12,098, doi:10.1029/1999JD900040.
- Turner, D. D. (2008), Ground-based infrared retrievals of optical depth, effective radius, and composition of airborne mineral dust above the Sahel, *J. Geophys. Res.*, **113**, D00E03, doi:10.1029/2008JD010054.
- Volz, F. E. (1973), Infrared optical constants of ammonium sulfate, Sahara dust, volcanic pumice, and flyash, *Appl. Opt.*, **12**(3), 564–568, doi:10.1364/AO.12.000564.
- Wald, A. E., Y. J. Kaufman, D. Tanré, and B.-C. Gao (1998), Daytime and nighttime detection of mineral dust over desert using infrared spectral contrast, *J. Geophys. Res.*, **103**(D24), 32,307–32,313, doi:10.1029/98JD01454.
- West, R. A., L. R. Doose, A. M. Eibl, M. G. Tomasko, and M. I. Mishchenko (1997), Laboratory measurements of mineral dust scattering phase function and linear polarization, *J. Geophys. Res.*, **102**(D14), 16,871–16,881, doi:10.1029/96JD02584.
- Yang, S., et al. (1999), Modified correlated k-distribution methods for remote sensing applications, *J. Quant. Spectrosc. Radiat. Transf.*, **64**, 585–608, doi:10.1016/S0022-4073(99)00140-5.
- Yoshioka, M., et al. (2007), Impact of desert dust radiative forcing on Sahel precipitation: Relative importance of dust compared to sea surface temperature variations, vegetation changes, and greenhouse gas warming, *J. Clim.*, **20**, 1445–1467, doi:10.1175/JCLI4056.1.

C. Gautier, P. Ricchiazzi, and M. Thomas, Institute for Computational Earth System Science, Department of Geography, University of California, Santa Barbara, CA 93106, USA. (matt.thomas@atk.com)